NTNU | Faculty of Information Technology and Electrical Engineering
Department of Electronic Systems

FACULTY OF ENGINEERING AND ARCHITECTURE

PROPERTIES OF CHANNEL AGING IN MASSIVE MIMO FOR RICH SCATTERING ENVIRONMENTS

MASTERTHESIS

Margot Niels
Student number (UGent): 01602198
Student number (NTNU): 533399

Supervisor: professor T. Ekman
Promotor: professor dr. ir. J. Verhaevert

Academic year: 2019-2020

NTNU
Norwegian University of Science and Technology

GHENT UNIVERSITY

NTNU | Faculty of Information Technology and Electrical Engineering
Department of Electronic Systems

FACULTY OF ENGINEERING AND ARCHITECTURE

PROPERTIES OF CHANNEL AGING IN MASSIVE MIMO FOR RICH SCATTERING ENVIRONMENTS

MASTERTHESIS

Margot Niels
Student number (UGent): 01602198
Student number (NTNU): 533399

Supervisor: professor T. Ekman
Promotor: professor dr. ir. J. Verhaevert

Academic year: 2019-2020

NTNU
Norwegian University of Science and Technology

GHENT UNIVERSITY

Acknowledgements

In order to successfully finalize this master thesis, I have got a lot to of help from several people that I want to thank for their help during my journey. First and foremost I would like to thank my guide and supervisor professor Torbjörn Ekman from NTNU for his good guidance, constructive discussions and feedback. I am also grateful for the opportunity professor Jo Verhaevert from UGent gave me to complete this master thesis abroad. Furthermore, I would like to thank Amy Landau for guiding me through the administrative web of the university and giving me solid start blocks to take off. Also, Jens Abraham deserves some credits for always being available for some questions and for giving the necessary advice and guidance. Also, Ingulf Helland and his team deserve a word of thanks for their pursuit to get the measurement equipment ready in time.

Next, I would also like to say a word of thanks to my fellow master students at the master's office for the good company before the lockdown and my flatmates to provide some distraction now and then during the lockdown. Last but not least, I want to thank my family for the moral support and more particularly my siblings for the tinkering at the plots and the second opinion at the writing.

Margot Niels, Trondheim, July 2020

Abstract

Channel aging is a troublesome aspect of Massive MIMO as it forces the base station to learn the characteristics of the channel over and over. This thesis investigates the behaviour of a rather uncomplicated environment under channel aging with the aim of contributing to a better understanding of this phenomenon for Industrial IoT. The theoretic models will be verified with geometry-based models that mimic as well as possible a real situation without requiring too much computational complexity. The setup that was meant to be used for the measurements (that were not carried out thanks to the Corona-situation) is used as an inspiration to create a realistic environment. As the simulations take place in two dimensions, some of those settings (e.g. the antenna spacing, the number of base station antennas) might turn out not to be the best choice.

Table of contents

List of figures

List of tables

1 Introduction

Massive Multiple Input Multiple Output (MIMO), also called Large-Scale Antenna Systems, is a technology that still needs some research in order to fully understand its behaviour in all situations. This thesis investigates some aspects of the behaviour of this system in an Industrial Internet of Things (IIoT) environment as, to the best of our knowledge, this field is not explored to the fullest yet. In contrast with a mobile communication environment, in an IIoT environment, the base station (BS) stands close to the user equipments (UEs) and there are much more UEs that need to be served at the same time. Therefore, not all properties from an ordinary Massive MIMO-system apply in this situation.
More particularly the aspect of channel aging is researched. There is a need to know how fast the communication channel between a BS a UE decorrelates as this affects the functionality of the UE itself. If the channel decorrelates more rapidly with the movement of the UE, the knowledge on this channel gets outdated faster and more resources are needed to learn the channel characteristics again. On the other hand, with a fast decorrelating channel, other UEs can move much closer to the intended UE without experiencing a significant amount of interference.
Initially, these characteristics were going to be measured with the equipment from the ReRaNP project [1]. However, as 2020 will go down in history as the year of hand sanitizer and lockdowns, the plans have been changed to simulation-based research. The software for those simulations will be developed and then used to observe the behaviour in the intended environment.

This thesis is further organized as follows: in Chapter 2 the main principles of Massive MIMO that are also needed for the simulations, like precoding techniques and channel calculation, will briefly be explained. Chapter 3 focusses on the simulations, what they represent and what came out of them. Both a stochastic model as well as a deterministic model will be discussed. The former is treated to form a thought on what might be expected from the latter. Chapter 4 concludes the thesis with a summary of the results and some thoughts on future works.

2 Massive MIMO principles

The Massive MIMO technology contains a lot of principles. In this chapter, the main principles, that are also needed for the simulations later on, are clarified shortly. Some specific properties of the use of Massive MIMO in IIoT environments will be discussed as well.

2.1 Technology and model

There is no fixed definition for Massive MIMO as the definition differs with the application. A possible definition for Massive MIMO could be as follows: Massive MIMO is a scalable

version of the multi-user MIMO (MU-MIMO) technology with, in most cases much more antennas at the BS then there are UEs in the cell. It uses space-division multiple access (SDMA) to serve the different UEs at the same time through a channel with asymptotically favourable propagation, in most cases with time division duplexing (TDD) to separate the uplink from downlink. Linear precoding and decoding multiplexing are employed, which only need the Channel State Information (CSI) in the downlink. [2] [3]
Such a definition might look overwhelming as it tries to cover as many key properties as possible. The mooted properties will be broken down bit by bit in following subsections.

2.1.1 The base station and user equipment

The BS consists of M antennas, while there are K UEs in the cell. For the sake of simplicity, each UE is supposed to be equipped with only one antenna. Theoretically, the performance of Massive MIMO gets better when the ratio M/K gets bigger. In most cases M is therefore much larger than K. However, this is not a must: K can even be larger than M. In order to increase the number of UEs, one might introduce intra-cell reuse of pilots. [4] If the reuse of pilots still isn't enough, time-frequency scheduling can then be introduced to cope with traffic peaks. [2]

There are some advantages of M growing large: the capacity and spectral efficiency grow as the number of degrees of freedom (DoF) grows, the array gain grows, a decrease in presence of inter-user interferences (IUI) and channel hardening[1] is introduced. The disadvantages of a big number of antennas in an array can include complex hardware, mutual coupling and more time lost by estimating the downlink channel. In practical cases, M would be between 100 and 200 as adding more antennas would not improve the performance much more, but the complexity of the hardware and such would still grow. [5]

UEs are generally randomly distributed over the considered area. The BS can have some different setups. Mostly it is chosen to be linear, cylindrical or planar. In a linear configuration, the array becomes really long, very quick. It, therefore, has a big aperture and thus a bigger near-field. In contrast to the far-field, there is no planar, but spherical wavefront in the near-field. The BS can, therefore, identify both the incident angle and the propagation distance from the user or scatterer, while with planar waves only the incident angle can be found. Besides, it has a bigger angular resolution in a linear formation. And it is easier to simulate as it only works in two dimensions.
If a cylindrical setup is chosen, the array is more directive and three dimensions are possible, but the angular resolution will be smaller. If polarised antennas are used, the array can also support polarisation diversity.
With a planar configuration, it has more or less the same properties, but it is easier to

[1] The more antennas the BS has, the more 'eyes' it has on the channel. The channel response is averaged out over all BS antennas. The variation of the channel response, therefore, decreases as M increases. It also ensures that the SNR is more stable at the UE.

mount the array to a wall or the ceiling which makes it very suitable for indoor applications.

2.1.2 Channel calculation

A signal that is sent over a wireless communication channel is affected by the medium and the nature of the surrounding area through which it travels. These effects are bundled together in what is called the channel response. A wireless channel can be interpreted as a linear, time-varying system. [6] The equation describing the output $\mathbf{y} \in \mathbb{C}$ of this system is given by:

$$\boldsymbol{y}(t) = \boldsymbol{h}(t)\boldsymbol{s}(t) + \boldsymbol{n}(t) \qquad (1)$$

where $\boldsymbol{h} \in \mathbb{C}^M \sim \mathcal{N}_{\mathbb{C}}\,(0,1)$ is the channel response, $\boldsymbol{s} \in \mathbb{C}^M$ the input signal and $\boldsymbol{n} \in \mathbb{C}^M \sim \mathcal{N}_{\mathbb{C}}\,(0, \sigma_n^2)$ the spatially white additive Gaussian noise.

If the channel response from a UE on a certain point x is known, the channel response from a UE in another point on a distance Δx from the original point can be written as:

$$\boldsymbol{h}(x+\Delta x) = \rho(\Delta x)\boldsymbol{h}(x)+\sqrt{1-\rho^2(\Delta x)} \qquad (2)$$

In the case of a classical spectrum with Rayleigh fading, the correlation function ρ corresponds with the Bessel function of the first kind and the zeroth-order [7]:

$$\rho(\tau) = J_0(2\pi f_m \tau) \quad \text{with: } \tau = \frac{\Delta x}{c} \text{ and } f_m = \frac{c}{\lambda}$$

$$\Rightarrow\ \rho(\Delta x) = J_0\left(2\pi\frac{\Delta x}{\lambda}\right) \qquad (3)$$

This theoretical approach does not take any properties of the environment into account and is therefore called a stochastic, correlation-based model. However, to make simulations closer to reality, a deterministic geometry-based model would be a better choice.

A deterministic geometry-based model is based on propagation mechanisms in a certain environment (e.g. ray-tracing or EM-wave theory). Also, the geometry of the environment is taken into account. This makes this kind of models very reliable, but also computationally more complex. In the following paragraph, such a model for a rich scattering environment will be unveiled.

In a rich scattering environment, the signal travels via multiple paths. A path can be defined as a single input single output (SISO) link between a UE and one of the BS antennas. One of those paths is shown in Figure 1.

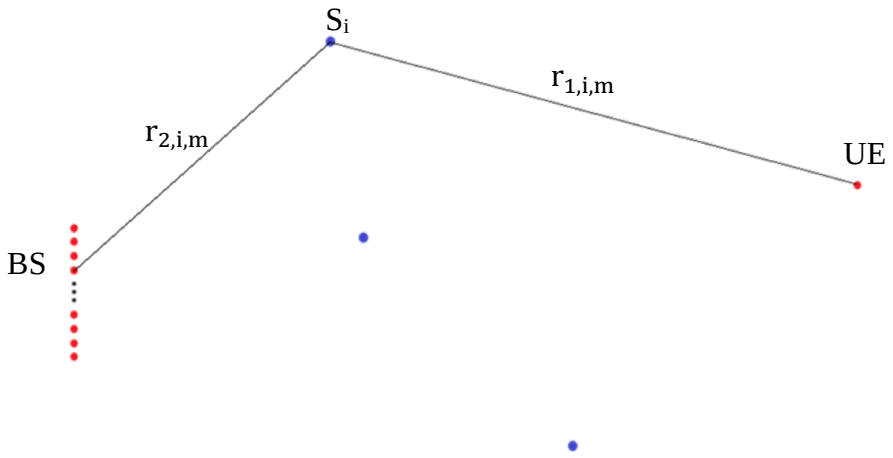

Figure 1: propagation path in a rich scattering environment from the UE to the m[th] antenna in the BS through the i[th] scatterer

The channel response of the system is influenced by all possible paths from the UE to the BS and can be written as:

$$\boldsymbol{h} = [\boldsymbol{h}_1, \boldsymbol{h}_2, \dots, \boldsymbol{h}_m, \dots, \boldsymbol{h}_M] \quad (4)$$

and

$$\boldsymbol{h}_m(x) = \sum_i^S a_i e^{-j\theta_i} \quad (5)$$

where a_i is the attenuation and θ_i represents the phase shift attributed to path i [6]. The number of paths is equal to the number of scatterers times the number of BS-antennas (SxM). The phase shift θ_i is determined by the total pathlength d_i and can be written as:

$$\theta_i = 2\pi \frac{d_i}{\lambda} \quad (6)$$

where λ is the wavelength of the carrier wave[2]. The total pathlength d_i for the path shown in Figure 1, would be $r_{1,i,m} + r_{2,i,m}$ where i denotes the i[th] scatterer and m the m[th] antenna in the BS. For the attenuation a_i, any path loss model can be used. The easiest path loss model is the one for free space which can be deduced from the Friis transmission equation [8], [9]:

$$PL = \frac{P_r}{P_t} = \left(\frac{\lambda}{4\pi R}\right)^2 \quad (7)$$

where P_r and P_t are the received and transmitted power respectively and R the distance between the transmitter and the receiver. All polarisation losses are neglected and antenna efficiencies and directivity are assumed to be maximal.
If the signal passes through a lossless scatterer, the scatterer acts as a point source that

[2] A wave of fixed amplitude and frequency that is modulated in amplitude, frequency, or phase in order to carry a signal in radio transmission [21]

retransmits every incoming wave without distorting it. The relation between power in the scatterer P_s and the transmit (at UE) or receive (at BS) power can then be written as:

$$a_{1,i} = \frac{P_s}{P_t} = \left(\frac{\lambda}{4\pi \mathrm{r}_{1,\mathrm{i,m}}}\right)^2 \quad (8)$$

$$a_{2,i} = \frac{P_r}{P_s} = \left(\frac{\lambda}{4\pi \mathrm{r}_{2,\mathrm{i,m}}}\right)^2 \quad (9)$$

From Eqs. (8) and (9) follows:

$$a_i = \frac{P_r}{P_t} = \left(\frac{\lambda}{4\pi}\right)^4 \left(\frac{1}{\mathrm{r}_{1,\mathrm{i,m}} \mathrm{r}_{2,\mathrm{i,m}}}\right)^2 \quad (10)$$

Out of Eqs. (5), (6) and (10), the channel response can now be written as:

$$\boldsymbol{h}_{m,scat} = \left(\frac{\lambda}{4\pi}\right)^4 \sum_{i=1}^{S} \left(\frac{1}{\mathrm{r}_{1,\mathrm{i,m}} \mathrm{r}_{2,\mathrm{i,m}}}\right)^2 e^{-j2\pi \frac{d_i}{\lambda}} \quad (11)$$

In case the waves would not travel through scatterers, but via a reflection on walls or another obstacle, the channel response would look like:

$$\boldsymbol{h}_{m,refl} = \left(\frac{\lambda}{4\pi}\right)^2 \sum_{i=1}^{S} \left(\frac{1}{\mathrm{r}_{1,\mathrm{i,m}} + \mathrm{r}_{2,\mathrm{i,m}}}\right)^2 e^{-j2\pi \frac{d_i}{\lambda}} \quad (12)$$

In a real environment most likely a mix of both Eqs. (11) and (12) will have to be applied.

Other, more complex, path loss models will not further be discussed in this thesis as they are not used in the simulations. Such models can, for example, be found in the ITU recommendations.

2.1.3 Asymptotically favourable propagation

A channel has favourable propagation if the channel vectors of all users $\boldsymbol{h}_k$ are mutually orthogonal so that:

$$\boldsymbol{h}_k^H \boldsymbol{h}_i = 0 \quad \text{with: } k, i \in [1, K] \ \wedge \ k \neq i \quad (13)$$

In that way, all users can be served at maximal capacity at the same time. However, in practice, the channels are hardly ever orthogonal. Therefore ‘asymptotically’ refers to the following property of large arrays:

$$\lim_{M \to \infty} \frac{1}{M} \boldsymbol{h}_k^H \boldsymbol{h}_i = 0 \quad (14)$$

This can also be seen by looking at the beamforming for arrays with large M. The beams that are formed at a BS with a larger M are much smaller than the beams that were formed with a smaller M. It is, therefore, possible to serve each user separately with SDMA.

2.1.4 Time division duplexing vs frequency division duplexing

The main difference between TDD and FDD is the number of symbols that are used in each coherence block[3] to estimate the channel. In the following paragraphs, the estimation procedure will be briefly described. [2], [3]

2.1.4.1 Frequency division duplexing

If an FDD system is used, the uplink (i.e. from UEs to BS) channel and the downlink (i.e. from BS to UEs) channel are separated in frequency. To estimate the uplink channel response, $\tau_u \geq K$ pilot symbols are used. For the estimation of the downlink channel response, $\tau_d \geq M$ pilot symbols are sent from the BS. Thereafter, the K UEs transmit the M received pilot symbols back as a feedback mechanism. This makes the total amount of used symbols for channel estimation:

$$\tau_{pilot} = \tau_u + 2\tau_d \geq K + 2M. \quad (15)$$

2.1.4.2 Time division duplexing

In a TDD system, the uplink channel and the downlink channel are separated in time. The system would again need $\tau_u \geq K$ pilot symbols to estimate the uplink channel response. Due to channel hardening in Massive MIMO, the channel responses of the uplink and downlink are reciprocal. This reciprocity eliminates the need for downlink pilots as the uplink and downlink channel responses are asymptotically the same. The total amount of used symbols for channel estimation would now be:

$$\tau_{pilot} = \tau_u \geq K \quad (16)$$

TDD is widely more used in the Massive MIMO technology as the number of symbols needed for CSI estimation is much smaller than with FDD, which leaves more symbols available for payload data. FDD for Massive MIMO is nevertheless an important subject for research as previous technologies made more use of FDD. [10] TDD has also some other drawbacks: lower signal-to-noise ratio (SNR) than FDD; larger guard periods in larger cells as the delay spreads differ more between different UEs; and uplink/downlink synchronisation between neighbouring BS's. [11]

2.1.5 Precoding and decoding

All processing is done by the BS to make the UEs as cheap as possible. As both the transmitted and received signals are affected by the channel, the BS tries to undo these effects by applying precoding to the outgoing signals or decoding the incoming signals. It

[3] A coherence block is a time/frequency block in which the channel is approximately the same. The dimensions of such a block are given by the coherence bandwidth B_c and the coherence time T_c. The total amount of available transmission symbols is thus $\tau_{tot} = B_c T_c$.

does so by multiplying the incoming/outgoing signal with a well-chosen weight $\boldsymbol{w}_k$. The uplink signal that is received and processed at the BS $\hat{\boldsymbol{y}}_k$ would then look like:

$$\hat{\boldsymbol{y}}_k = \boldsymbol{w}_k^H \boldsymbol{y}_{k,UL} = \underbrace{\boldsymbol{w}_k^H \boldsymbol{h}_k \boldsymbol{s}_k}_{desired\ signal} + \underbrace{\sum_{\substack{i=1 \\ i \neq k}}^{K} \boldsymbol{w}_k^H \boldsymbol{h}_i \boldsymbol{s}_i}_{Intra-cell\ interference} + \underbrace{\boldsymbol{w}_k^H \boldsymbol{n}}_{noise} \qquad (17)$$

where $\boldsymbol{h}_k$ is the channel vector of the k[th] user, $\boldsymbol{n}$ denotes the noise and $\boldsymbol{s}_k$ the uplink (mostly n-QAM modulated) signal that was sent from the k[th] UE. If $\boldsymbol{w}$ is chosen well, $\boldsymbol{w}_k^H \boldsymbol{h}_k = 1$, causing $\hat{\boldsymbol{y}} = \boldsymbol{s}_k$ assuming that there would be no noise or interference.
In the downlink, the weights are applied before the signal is sent. The signal that is received at the UE would then look like:

$$\boldsymbol{y}_{k,DL} = \underbrace{\boldsymbol{h}_k^H \boldsymbol{w}_k \boldsymbol{\varsigma}_k}_{desired\ signal} + \underbrace{\sum_{\substack{i=1 \\ i \neq k}}^{K} \boldsymbol{h}_k^H \boldsymbol{w}_i \boldsymbol{\varsigma}_i}_{Intra-cell\ interference} + \underbrace{\boldsymbol{n}_k}_{noise} \qquad (18)$$

where $\boldsymbol{\varsigma}_k$ stands for the downlink (mostly n-QAM modulated) signal that was sent to the k[th] UE. Again, if $\boldsymbol{w}$ is chosen well, $\boldsymbol{h}_k^H \boldsymbol{w}_k = 1$ resulting in $\boldsymbol{y}_{k,DL}$ to equal $\boldsymbol{\varsigma}_k$ neglecting noise or interference. [2]

In contrast to MU-MIMO that uses dirty-paper (de)coding, Massive MIMO uses linear precoding and decoding techniques. The linear pre- and decoding techniques do not need the downlink channel estimation as was the case with the dirty-paper (de)coding. This makes the efficiency of Massive MIMO independent of M, and thus scalable.

There are three widely used pre-/decoding schemes: Maximum Ratio Combining (MRC), Zero-Forcing (ZF) and Minimum-Mean-Squared-Error (MMSE). Their properties are explained in the subsequent paragraphs.

2.1.5.1 Maximum Ratio Combining

MRC, also called MR transmission (MRT) or Matched Filtering (MF), causes constructive interference at the desired UE so that the SNR to each user is maximised. This property makes MRC very suitable for noisy environments. After gathering the CSI from the uplink pilots, the channel responses of all users are known. MRC uses these channel responses $\boldsymbol{h}_k$ as a weight $\boldsymbol{w}$ for precoding and decoding [2]:

$$\boldsymbol{w} = \boldsymbol{H} = [\boldsymbol{h}_1, \boldsymbol{h}_2, \dots, \boldsymbol{h}_k, \dots, \boldsymbol{h}_K] \qquad (19)$$

The downsides of this technique are that the IUI is ignored and that it needs much more antennas at the BS to reach optimal performance than the other techniques. [12]

2.1.5.2 Zero-Forcing

This technique aims for an IUI-free environment. Here, $\boldsymbol{w}_k$ is chosen to be $\boldsymbol{h}_k(\boldsymbol{h}_k^H \boldsymbol{h}_k)^{-1}$, so that destructive interference is introduced at the non-desired users. This technique is computationally much more complex as the large channel response matrix (containing all channel responses of all users) has to be used three times.[13] Another disadvantage of ZF is that the noise will be amplified in environments with a low SNR. This makes

ZF very unsuitable in noisy environments or when the orthogonality between users is poorly implemented. In environments where the SNR is high, the performance of the system is limited by IUI, so ZF would be a good choice.

2.1.5.3 Minimum-Mean-Squared-Error

MMSE uses the best of both worlds: it works well in both environments with low and high SNR. It tries to estimate the noise variance and feeds it back to the transmitter. The weight $\boldsymbol{w}$ is now chosen to be $\boldsymbol{h}_k(\boldsymbol{h}_k^H \boldsymbol{h}_k + \alpha \boldsymbol{I})^{-1}$ where $\alpha = \frac{K \sigma_n^2}{P_{Tx}}$ is the ratio of the transmitted symbol energy to the noise spectral density, with σ_n^2 as the noise-covariance and P_{Tx} as the transmitted power. It is easy to see that if $\alpha = 0$ (i.e. in case of high SNR), the ZF combining scheme is obtained. If $\alpha \to \infty$ (i.e. in case of low SNR), the formula converges to the MRC scheme. Although this is a good combining scheme that covers situations with both low and high SNR, it is not frequently used in the research literature as it has a very high computational complexity. [12]

2.1.6 Channel aging

The CSI that is needed for the processing at the BS will in practice not forever be constant. After some time, the acquired channel will no longer match the real channel due to user mobility or some changes in the environment as the channel decorrelates. [14] The phenomenon that describes the difference between the channel at the acquisition of the CSI and the channel at the use of the CSI is called channel aging. The area in which the UE can operate with the same CSI will further on be referred to as *the bubble*.

If the CSI is not reacquired regularly, channel aging may cause a compelling drop in the data rate. [15] It also affects the desired signal power to the UE and inter-cell interference. [14]

If the UE moves faster, the channel will get worse faster, but the more BS antennas, the longer it takes until the channel has to be re-evaluated. After a while, however, increasing M would not have much of an effect, while the complexity still rises. Furthermore, if the intended UE can move further while having the same CSI, other UEs will experience more IUI as the so-called bubbles get bigger. Therefore, a careful consideration has to be made when adding more antennas in a pursuit to save more resources.

2.2 IIoT in Massive MIMO

In an IIoT environment, there are many more UEs than BS antennas. The Massive MIMO networks must, therefore, support massive connectivity. IIoT UEs also require low energy usage at the UE, devices must have the possibility to be very cheap and the links must be reliable. The first and the last requirements are met by increasing M: the energy efficiency gets lower for more BS antennas and channel hardening makes the communication more reliable. [16], [17] The second condition is also met because as much processing as possible is done at the BS, which allows the UEs to be a bit more fatuous. In addition, IIoT devices mostly send only small packages of data. It would be a waste of resources if the overhead is

bigger than the payload data itself. It is thus recommended to keep the pilots as small as possible.
As mentioned earlier, to get more UEs connected without having to use enormous pilots, pilots can be reused within the cell or time-frequency scheduling can be introduced to cope with busy traffic. Research has also proven that MRC is more suitable for IIoT environment than ZF as it can support way more UEs at a time. [4] It is also obvious that a TDD system is more suitable for this kind of applications as it takes less time and resources for estimating the channel.

3 Simulations

The original objective of this thesis was to measure the channel aging in a realistic industrial environment. Due to circumstances however, the thesis has been converted to a theoretical project where simulations are executed based on theory. The original setup has been preserved as much as possible, although some simplifications are applied to lower the computational complexity of the simulations. In that way, the results can be used in future work to compare with reality.

In the first simulation, the previously described stochastic correlation-based model will be used to show what can be expected from the theory. Thereafter, a deterministic geometry-based model will be exploited as a more practical approach to realistic environments.
The next paragraphs will describe the main characteristics of the deterministic model and the goal of the simulations.

3.1 Simulation setup for the geometry-based model

In order to be able to compare different plots with different properties, the default setting that will be described in the next paragraphs will be set as a reference point. This default setup will be as close as possible to the measurement setup mentioned earlier.

3.1.1 Base Station

A single-cell system (i.e. only one BS) will be considered with one UE and hundreds of scatterers. [18] The BS consists of M = 128 antennas spaced at the critical spacing of $\frac{\lambda}{2}$. The spacing at the BS, planned to be used in the practical measurements, stands a bit higher at 0,62λ. The spacing in the simulation, however, is chosen as the minimum spacing that is favoured to achieve higher directivity in larger antenna arrays, to keep the array as compact as possible. [19] Another reason to choose for a $\frac{\lambda}{2}$ spacing is that in this way the grating lobes are avoided to appear in the antenna pattern. [9][20]
The BS in the simulations is also linear instead of the planar BS, meant for the measurements. Therefore, it is only functional in the azimuth plane and has a bigger aperture. As the measurement-BS is described to have low mutual coupling, the mutual coupling is also not taken into account in the simulations as this would make things

needlessly more complicated.
As mentioned earlier, an IIoT network wants to be able to connect as much UEs as possible. It, therefore, uses TDD to separate the uplink from the downlink and MRC for precoding and decoding. During the processing, the power is normalized with distributed time-reversal normalisation whereby the power is scaled by $\sqrt{M}$. [10]

3.1.2 Environment

The BS stands at the edge of an open space area in which 500 scatterers are randomly placed in an area of 700λ[4] by 700λ at the broadside of the BS. For the sake of simplicity, each path consists of at most one scatterer. The scatterers can represent point sources that just retransmit the incoming wave uniformly in all directions. They can be made more realistic by letting them represent uniformly radiating antennas that reproduce incoming waves with a certain random phase shift and random attenuation.
A rich scattering environment is used to avoid correlations and to take advantage of the fact that a rich scattering non-line-of-sight (NLOS) environment can be seen as the approximate form of favourable propagation. [21] Including a line-of-sight (LOS) would furthermore dominate the simulation, so to see the worst-case scenarios, the simulations are NLOS. The area is not enclosed by walls since, due to path loss, reflections from side walls are considered to be neglectable for a big area.
As the 128 BS antennas are spaced at $\frac{\lambda}{2}$ from each other, the far-field begins at $\frac{2D^2}{\lambda}$ = 8064.5λ, which means that the whole region is located in the near field.

3.2 The goal of the simulation

The simulations seek to paint a picture of the correlation between a certain location of a UE and the surrounding points. These surrounding points can represent the position of the same UE at another point in time or another UE at the same point in time but at a different location. The correlation between two points is measured by evaluating the difference in power that is received in both points.

The simulations that will be executed are the following: first, a theoretical simulation will be carried out in order to know what can be expected from the following simulations. Next, some simulations are done that describe a more practical environment as described in section 3.1. Within these simulations, some properties are tested, like the effect of M on the channel aging, the position of the UE and the effect of the placing of the scatters

[4] All distances are noted in function of λ to make the simulation independent of the used frequency.

3.3 Simulation results

3.3.1 Stochastic correlation-based model

In this model, the UE is located in open space. As a first step, M is defined along with the intended resolution (described with respect to λ). The final plot will always be of the same size (400x400 pixels), the resolution only helps to zoom in or out. Thereafter, M complex normal random variables are generated, that together form $\boldsymbol{h}(x) \in \mathbb{C}^M$. The weight vector $\boldsymbol{w}$ is then chosen to be equal to $\boldsymbol{h}$ and the Hermitian transposed is taken. Afterwards, $\boldsymbol{h}(x+\Delta x)$ is calculated using Eqs. (2) and (3), with Δx the distances to the middle of each pixel in a window of 400x400 and the received power from that pixel is calculated using:

$$P_r = \frac{1}{\sqrt{M}} \boldsymbol{h}(x)^H \boldsymbol{h}(x + \Delta x) \qquad (20)$$

A possible result coming out of this model is shown in Figure 2. It can be noted that rings appear with more or less the same shape as the Bessel function of the first kind and zeroth-order.

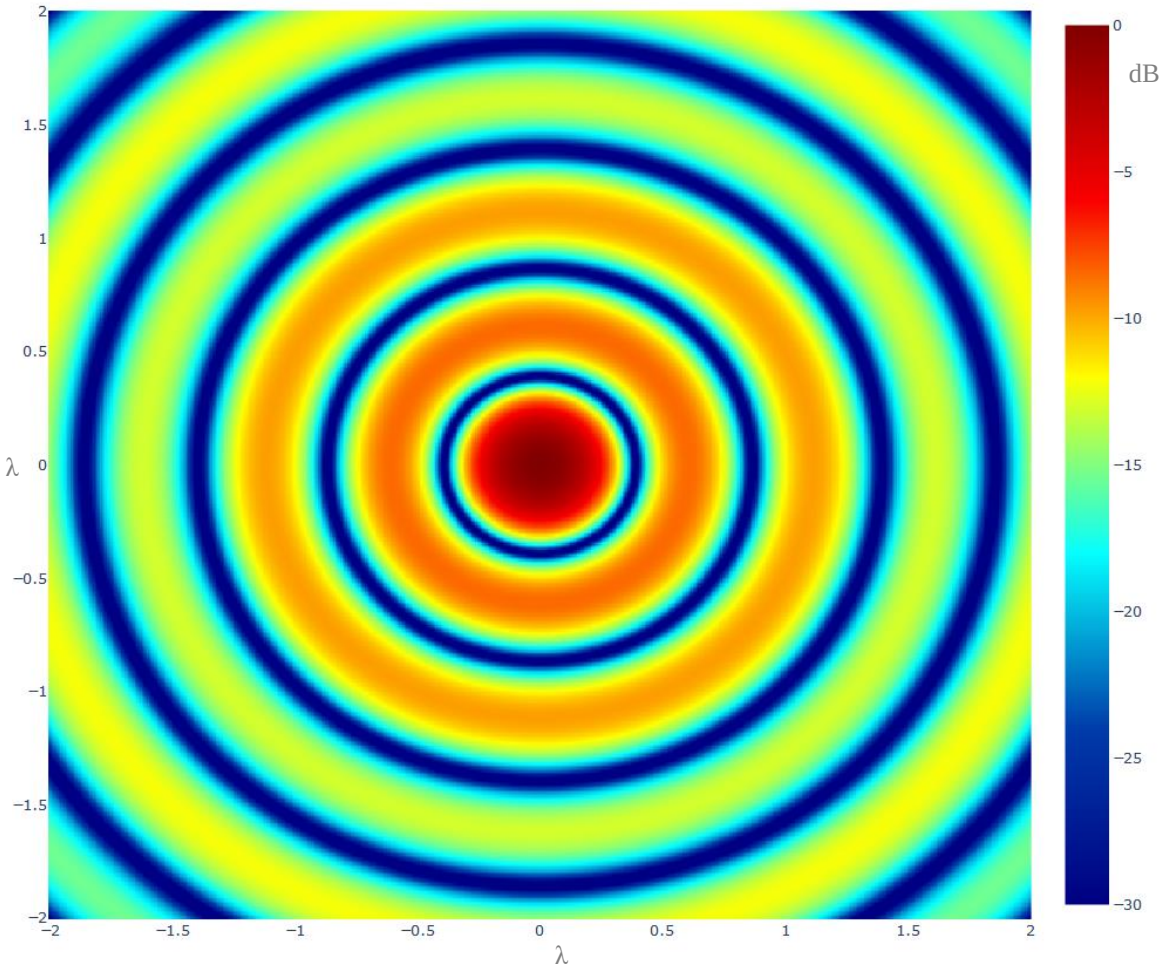

Figure 2: heatmap for a stochastic model with M=128 and resolution=0.01λ

These calculations can then be repeated for another 1000 times to eliminate the randomness of the channel response. In every version, the radius of the so-called bubble is

measured by looking for the first minimum in all directions with a precision of one degree. The histograms of the average radius of the bubble for M = 8, 16, 32, 64, 128, 256 is shown in Figure 3. The average of the 1000 averages and its variance are collected in Table 1, along with the average variance of the bubbles and the variance of the variances. It is however notable that there is a big amount of realisations that don't seem to have any bubble ($\Delta x = 0$). This happened because, in some versions, the values found first rose (approx. 0.02λ) before dropping down to expected levels. If those realisations would be left out, the variances and averages would be different. The numbers of the limited dataset are added to Table 1 under their corresponding values from the complete dataset. As the left-out results were equal to zero and had zero variance, it's easy to understand that the averages, as well as the variances, will now get higher. Except for the variance of the average: it can be intuitively seen that as the average coincides more with the mean of the dataset, the variance will be lower.

Table 1: radius of the bubble [$10^{-2}\lambda$]

M	8	16	32	64	128	256
avg. of avg.	18	19	21	22	24	28
avg. of avg. excl. 0	33	35	35	36	37	37
var of avg.	2.7	3.0	3.1	3.2	3.1	2.6
var of avg. excl. 0	0.18	0.11	0.11	0.11	0.10	0.17
avg. of var	0.022	0.032	0.045	0.072	0.066	0.11
avg. of var excl. 0	0.042	0.058	0.076	0.12	0.10	0.15
var of var	0.00065	0.00094	0.0013	0.0021	0.0020	0.0035
var of var excl. 0	0.0012	0.0017	0.0022	0.0034	0.0029	0.0045

The same analysis can then be made for the height of the bubble (i.e. the power received at the edge of the bubble relative to the power in the centre of the bubble). The results of this are assembled in Figure 4 and Table 2.

Table 2: height of the bubble [dB]

M	8	16	32	64	128	256
avg. of avg.	-8.962	-10.71	-13.11	-15.12	-17.85	-21.79
avg. of avg. excl. 0	-16.60	-19.30	-22.37	-24.62	-26.96	-28.67
var of avg.	101.4	122.6	157.0	173.2	193.3	181.6
var of avg. excl. 0	61.08	55.02	60.85	48.18	46.27	41.61
avg. of var	0.7421	1.029	1.863	3.638	4.188	7.505
avg. of var excl. 0	1.374	1.853	3.179	5.925	6.326	9.876
var of var	84.22	138.2	183.1	708.7	781.4	1539
var of var excl. 0	155.1	247.5	308.2	1141	1167	2001

Out of these numbers can be concluded that the size of the bubble grows with an increasing M, both in height and width. The CSI, therefore, has to be acquired fewer times when the UE is moving around if lower power drops are supported. The average variance also rises which tells us the bubble becomes a less perfect circle when M gets bigger. Looking at the histograms of the average bubble width, the variance seems to decrease for a higher M neglecting the bar of zeros. The numbers in Table 1 however, tell that the variance for 256 antennas is bigger than almost all the others. This can be explained by the bigger amount of outliers for that dataset, which in turn can be explained by the lower number of zeros ergo a bigger dataset.

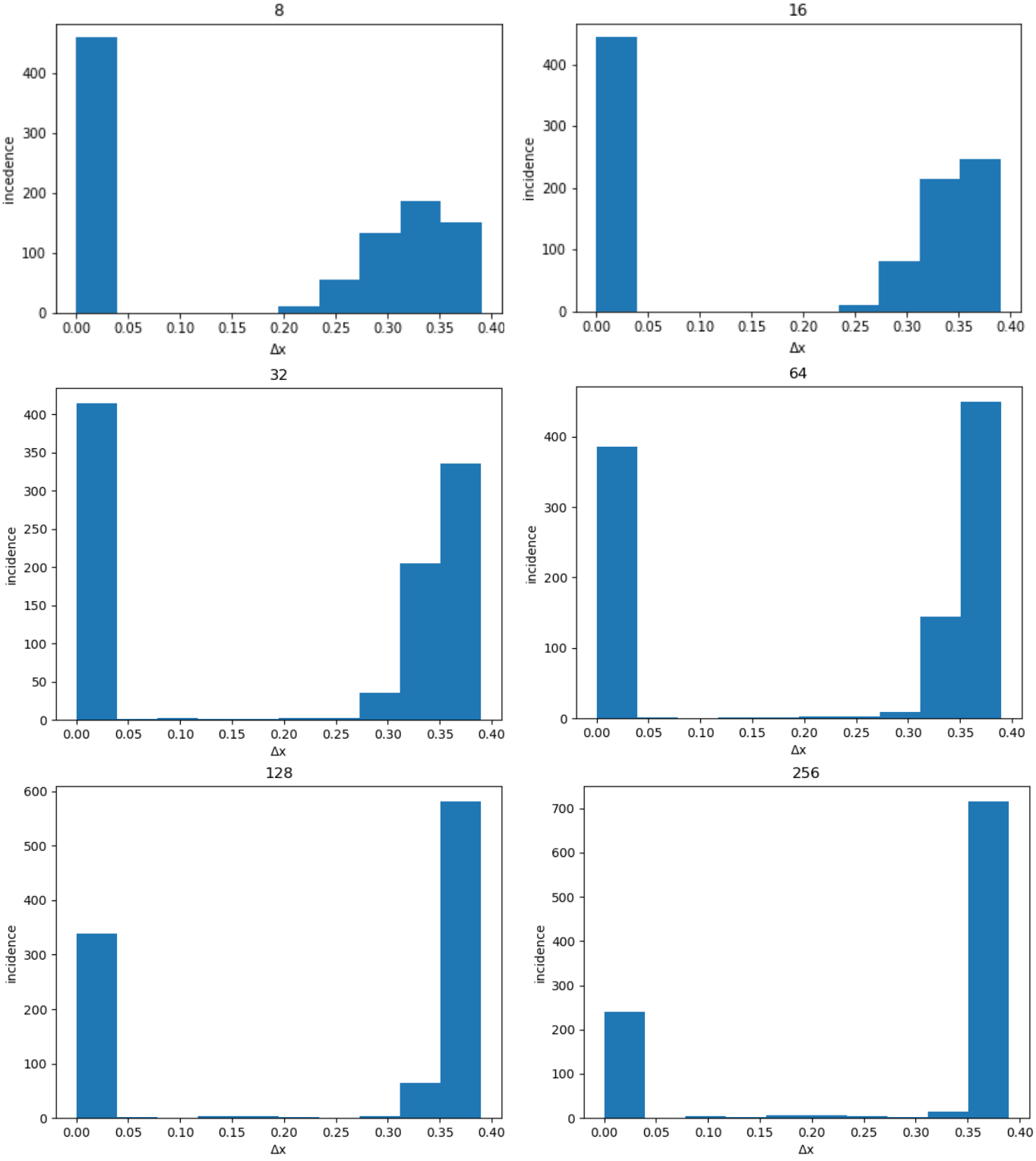

Figure 3: average radius of the bubble for M = 8, 16, 32 ,64, 128, 256

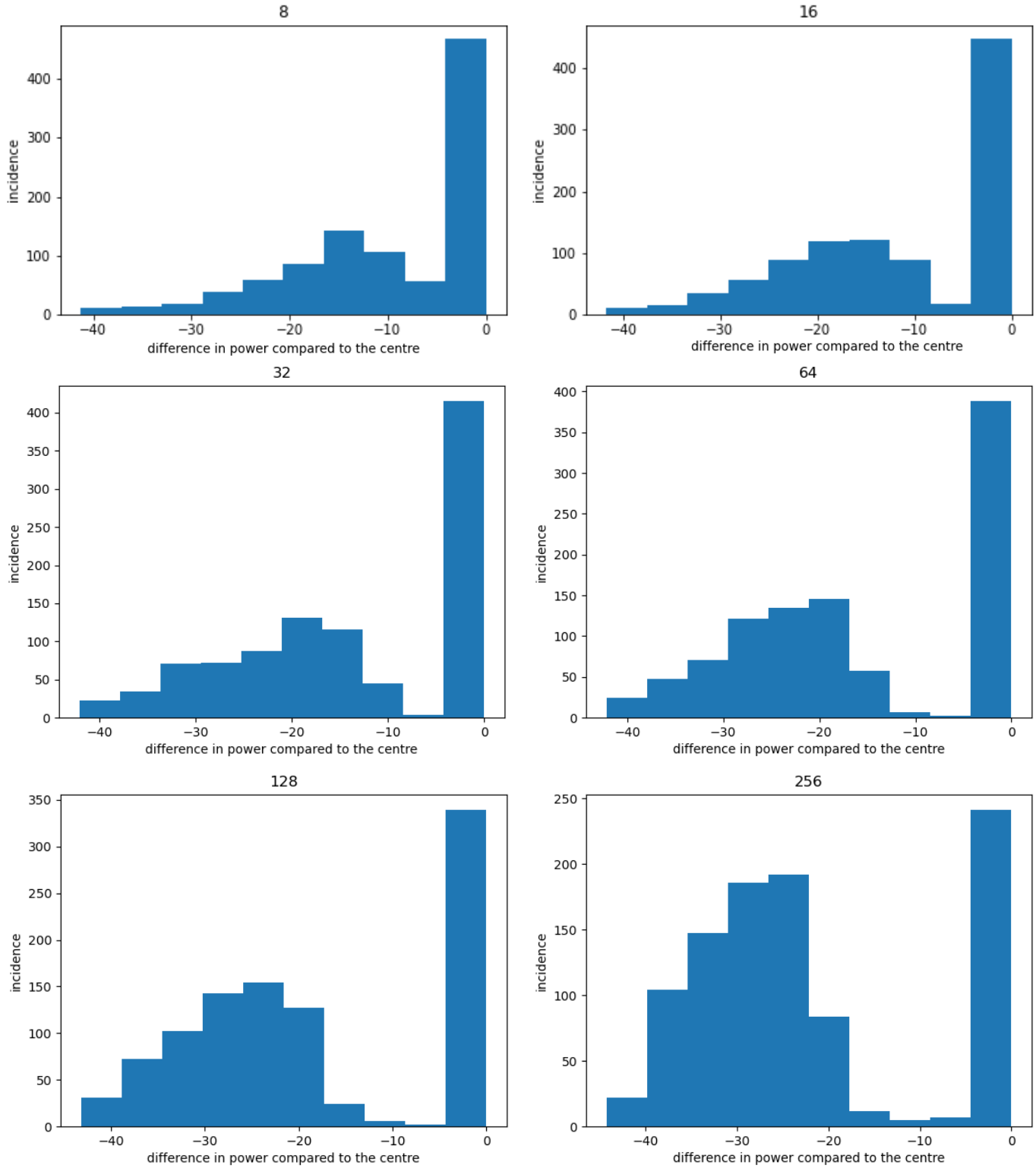

Figure 4: average height of the bubble for M = 8, 16, 32 ,64, 128, 256

3.3.2 Deterministic geometry-based model

The simulation setup from section 3.1 is now used to execute the deterministic geometry-based model. Every simulation can now differ in the number of BS antennas M, the distance between the BS antennas dM, placing of BS and scatterers, amount of scatterers S, region to be calculated, resolution, LOS included or not, the initial placement of the UE and how close the model stands to reality (whether or not to include a random loss and phase shift in the scatterers, include a path loss,…). The settings for a default situation were discussed before and are summarised in Table 3. The scatterers are placed on fixed locations throughout different realisations that are compared unless the placing of the scatterers itself has to be investigated. The UE is placed in front of the BS, more than 10λ away from the closest scatterer. A visualisation of this setup is exhibited in Figure 5.

Table 3: default settings of the deterministic geometry-based model

setting	value
M	128
dM	0.5
S	500
LOS	not included
placing of BS	vertically around [0, 400]
placing of scatterers	uniform distribution within 700λ x 700λ
initial position of UE	(354.62, 403.956)

The standard setup is then executed for an area of 40λ x 40λ around the UE and a resolution of 0.1λ. This means that the CSI is acquired for the initial position of UE using Eqs. (4)-(11), after which the right weight vector $\boldsymbol{w}$ is calculated. The received power on that spot is then proportional to $\frac{1}{\sqrt{M}}\boldsymbol{w}^{\mathrm{H}}\boldsymbol{h}$. Afterwards, the UE is moved 0.1λ and the channel vector $\boldsymbol{h}_{\mathrm{dx}}$ of that position is calculated. The correlation between those places corresponds to the difference in power, which is for this place calculated with the same weights as previously calculated, but with another channel vector: $\frac{1}{\sqrt{M}}\boldsymbol{w}^{\mathrm{H}}\boldsymbol{h}_{\mathrm{dx}}$. This is then done for the entire area of 20λ around the UE.

Figure 6 depicts the result of this procedure. What immediately stands out is the big amount of power that is received when the UE comes close to the scatterer. This might indicate that MRC is not the best choice after all as it doesn't take IUI into account. Other precoding schemas are not considered in these simulations but can be examined in future work. Another solution might be to not send any beams towards the scatterers that have another UE in the vicinity. Next to that, some beam-like patterns can be distinguished in the direction of the BS even though the UE is not positioned in the far-field.

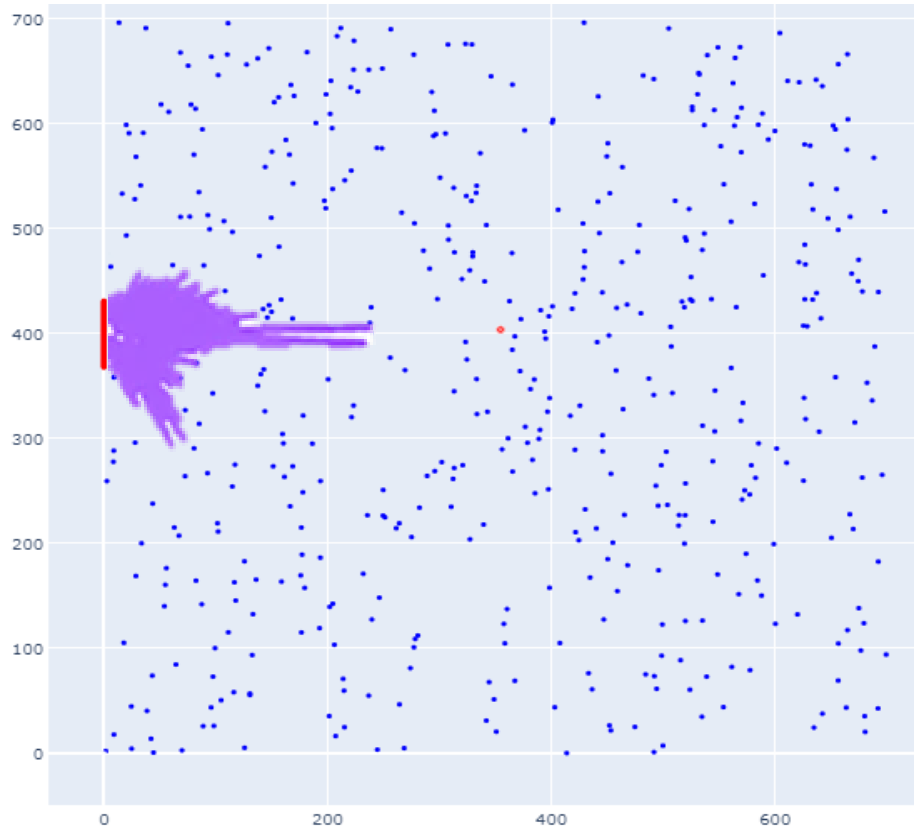

Figure 5: default setup for the deterministic geometry-based model where the BS is represented by the red line consisting of 128 dots at the left, the 500 scatterers by the blue dots and the UE by the red dot with a white cross in the middle. The purple plot is the antenna pattern and might cover some scatterers

In what follows, first, the effect of the number of antennas in the BS on the channel aging will be examined in the same way as the stochastic model. Then, dM will be variated and some different scattering placements will be explored. Those simulations are compared with the default situation. Finally, the behaviour of the system when the UE is moved to other places than the default place will be studied.

3.3.2.1 Number of base station antennas

The impact of the change in M is calculated in approximately the same way as the stochastic model. This time, however, the computational complexity is too high to recalculate the entire model 1000 times over. Therefore, the default model (with a different M) is first calculated and all channel vectors are stored. Then, a random point in the calculated area is chosen and the area is recalculated for that specific point. The bubble is measured next and finally, the data is stored. This procedure is then repeated another 998 times.

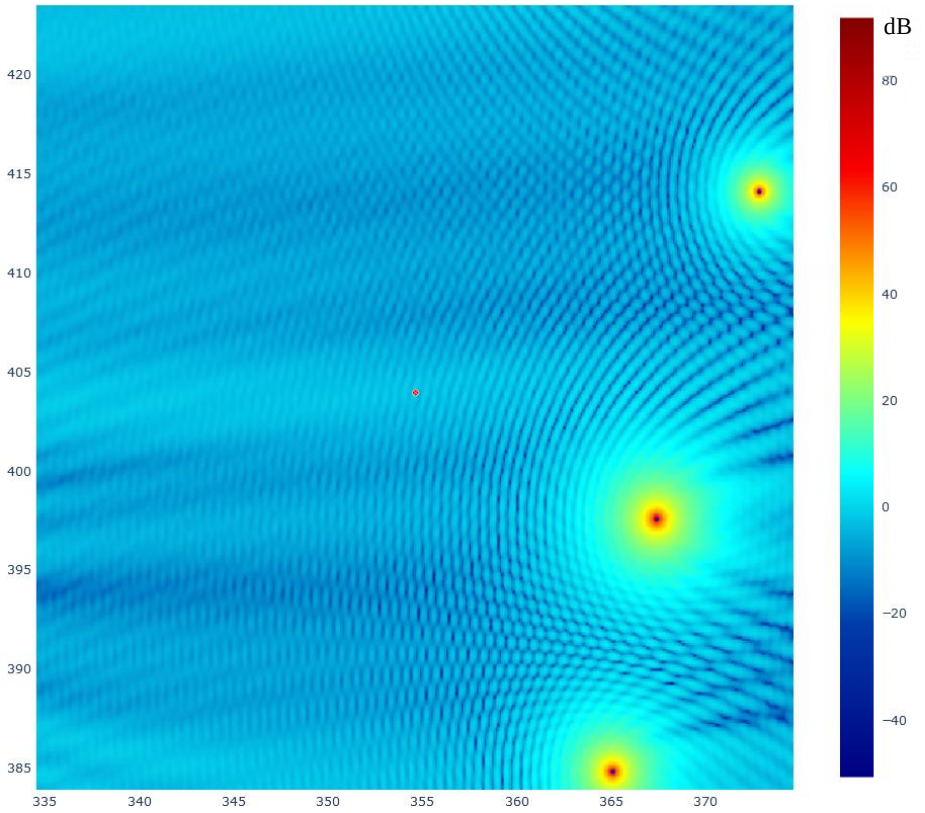

Figure 6: result for the default setup

By first precalculating the area around the default location of the UE, the computation time is reduced from forty hours per implementation to three seconds. The downside of this method, however, is that the plot is not formed around the UE anymore so the bubble might fall out of the plot. Those realisations are left out and replaced by another one. Another disadvantage of this approach is that only the area around the default UE position is investigated. Situations that only happen when the UE would, for example, be closer to the BS or not in front of the BS are not included.

The results of the simulations mentioned above are displayed in Table 4 and Table 5. Figure 8 and Figure 9 depict the histograms for the height and the width of the bubble.

Table 4: radius of the bubble [$10^{-2}\lambda$]

M	8	16	32	64	128	256
avg. of avg.	27	34	42	48	64	94
var of avg.	4.0	5.0	6.1	9.2	16	28
avg. of var	10	13	17	25	52	83
var of var	8.9	13	29	59	156	136

Table 5: height of the bubble [dB]

M	8	16	32	64	128	256
avg. of avg.	-3.962	-4.269	-4.611	-4.077	-4.469	-9,150
var of avg.	11.37	11.18	15.22	15.24	14.22	14,95
avg. of var	15.99	13.81	11.79	8.864	9.503	78,36
var of var	874.7	533.3	824.1	826.7	681.1	5384

The behaviour for M=256 stands out clearly in these simulations. This can be explained by the radiating near-field that starts only at 892.6λ, whereas for M≤128, it starts at 313.7λ or earlier. The behaviour of the UEs in the reactive near-field is different from their behaviour in the radiating near-field. [9] Also looking at the antenna patterns in Figure 7, all the patterns have a bigger beam in the direction of the UE, while in the pattern for M=256, this behaviour is less pronounced.

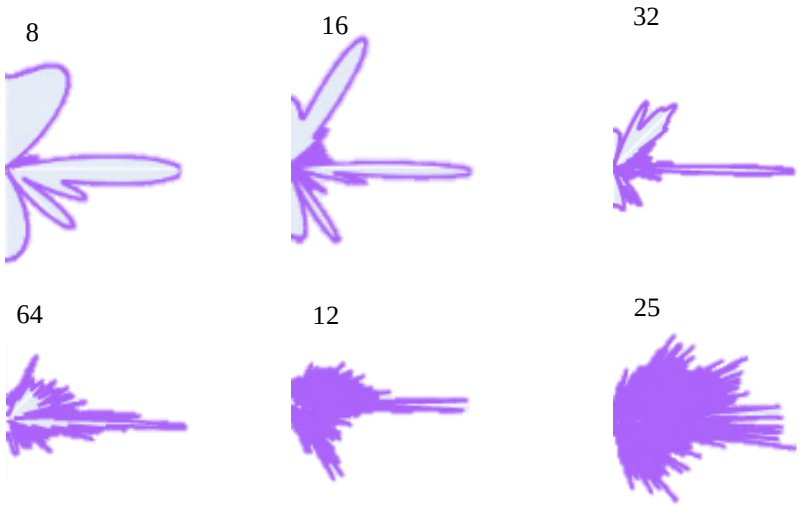

Figure 7: antenna patterns for M=8, 16, 32, 64, 128, 256

When the results of the deterministic model are compared to the results of the stochastic model, one can notice that the height of the bubble starts smaller, but grows much faster now. The width, however, turns out smaller and stays approximately the same for all versions except for the one with M=256.

When taking a closer look at the bubble in the default setup, the results shown in Figure 10 are a possible outcome. The shape from the bubble (indicated with the black markings) is anything but a circular shape, which can explain the large variances in the aforementioned results. However, the contours of the bubbles in Figure 10 are calculated in a different way than the ones in the dataset. If the edge of the bubble exceeds the calculated area, it is not considered as a failed plot, but rather a situation where the edge of the plot is considered to be the edge of the bubble. Also, the contours are added manually to the plots to make the designated areas more apparent. This manual addition might result in a reduction in accuracy (compared to an addition solely based on calculation), but this should not be of any major significance.

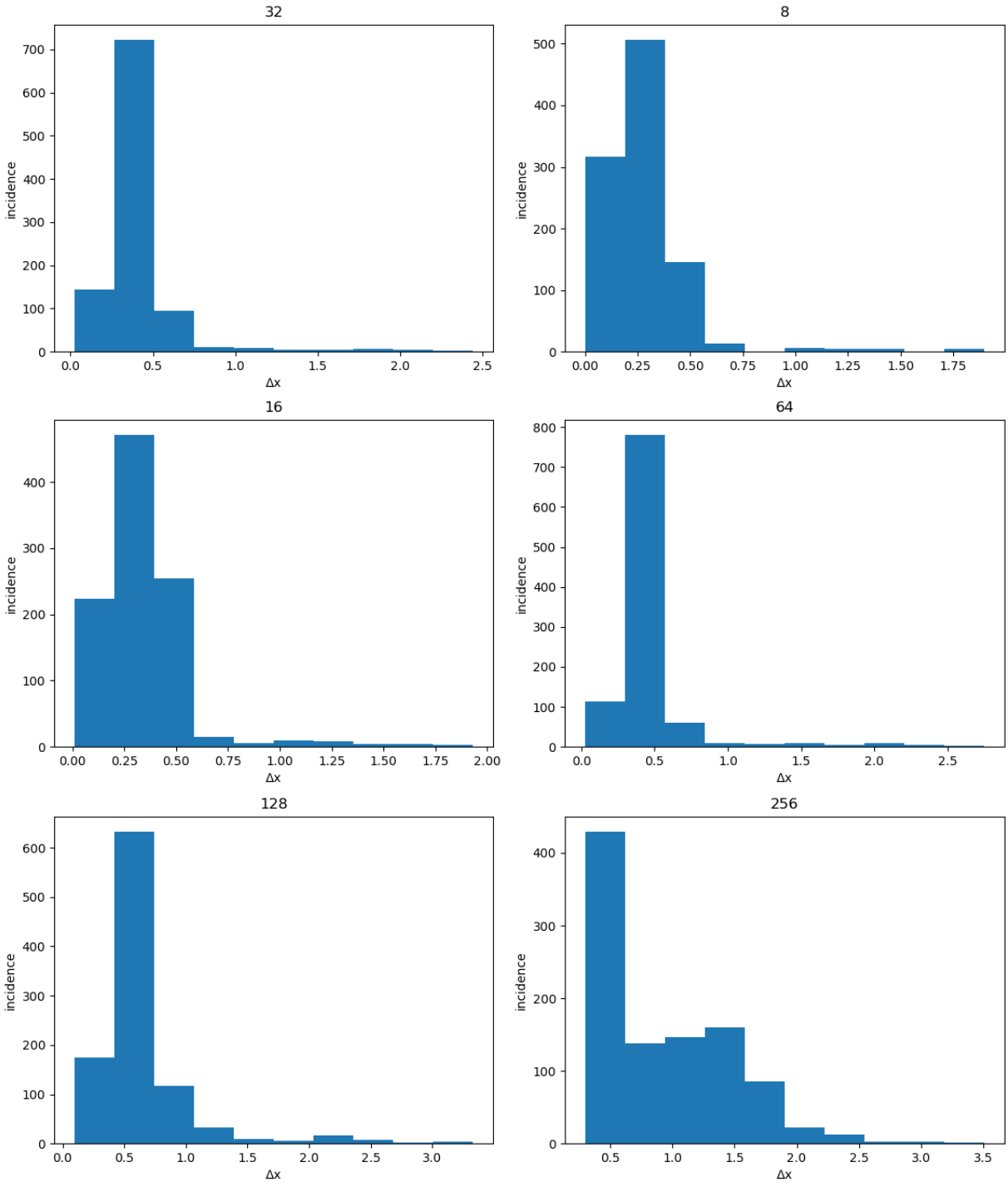

Figure 8: average radius of the bubble for M = 8, 16, 32 ,64, 128, 256

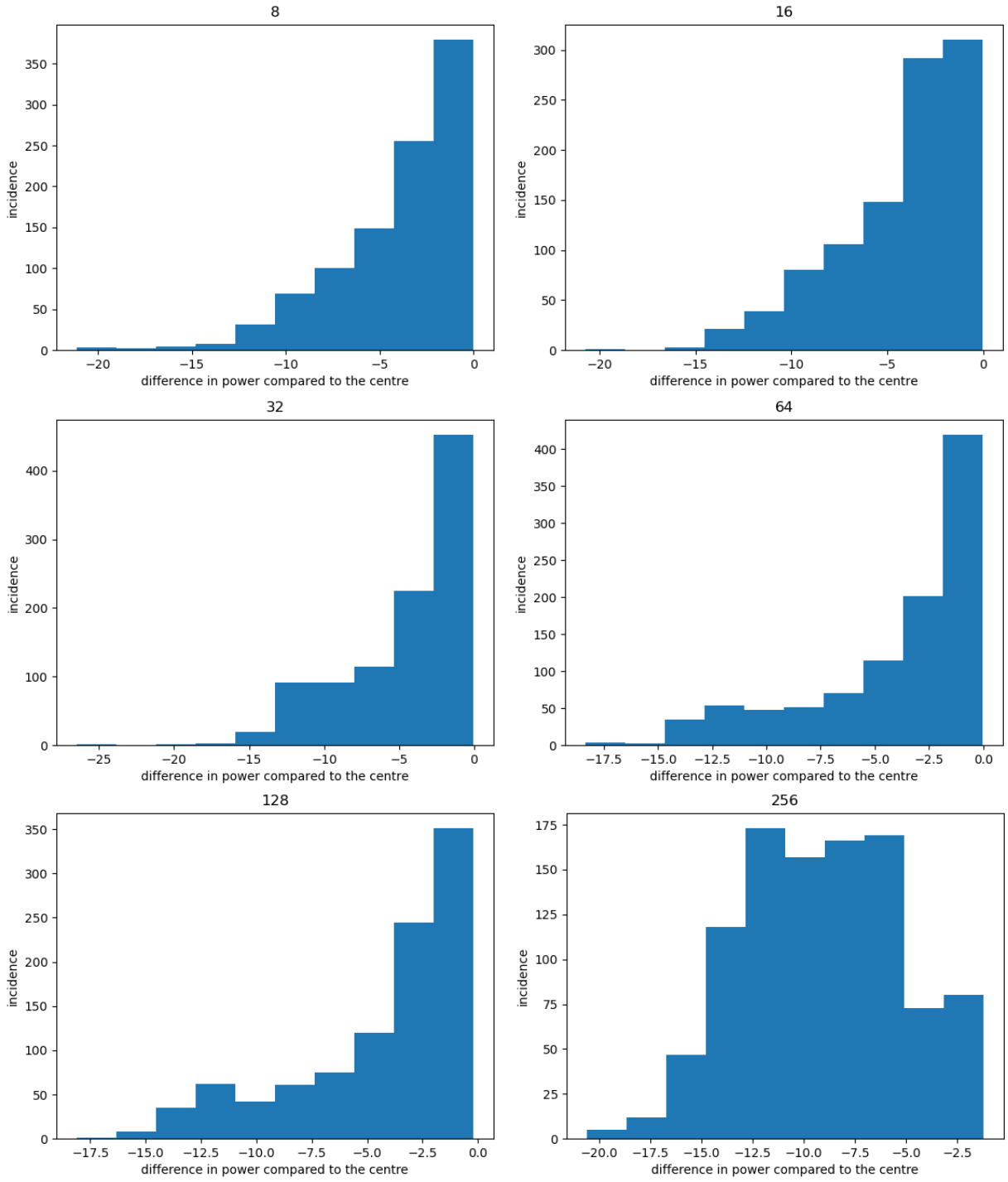

Figure 9: average height of the bubble for M = 8, 16, 32 ,64, 128, 256

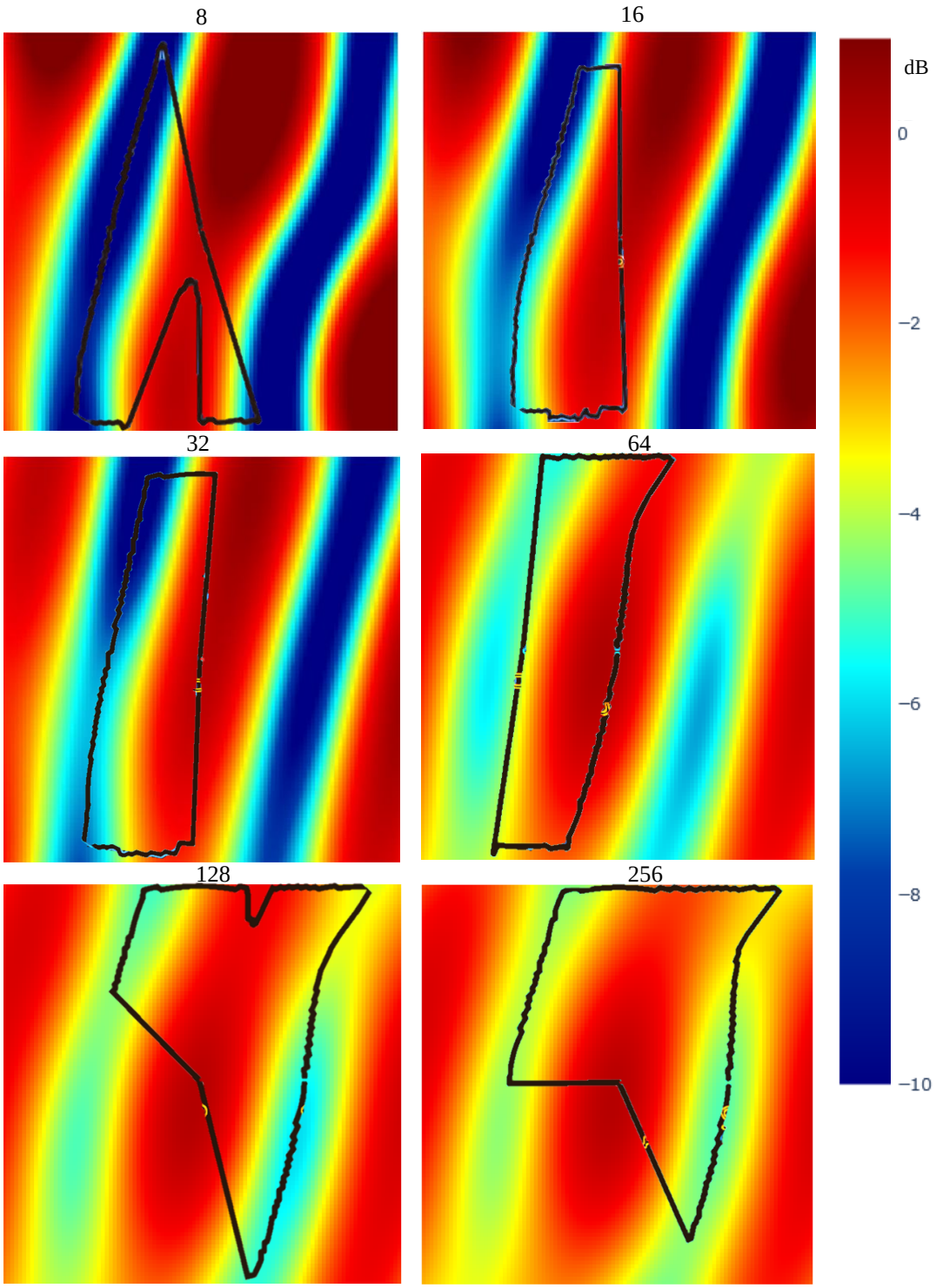

Figure 10: close-up of the bubble for M=8, 16, 32, 64, 128, 256. The black line depicts the contour of the bubble. All plots in are plotted 0.5λ around the default UE-position (354.62, 403.956) and share the same colour scale at the right.

The average power in all directions in function of the distance between the UE and the default position of the UE is compared with the Bessel function of the first kind and zeroth-order in Figure 11. It shows that the simulated model does not fall off as deep as the Bessel function, but it follows the Bessel function quite well. That the red line is less wobbly can be explained by looking at the previous plots (Figure 6 and Figure 10).

The bubble falls off fast in one direction, while in the other direction it almost remains stable. Since all directions are included in the plot, the hilly shapes are pronounced less.

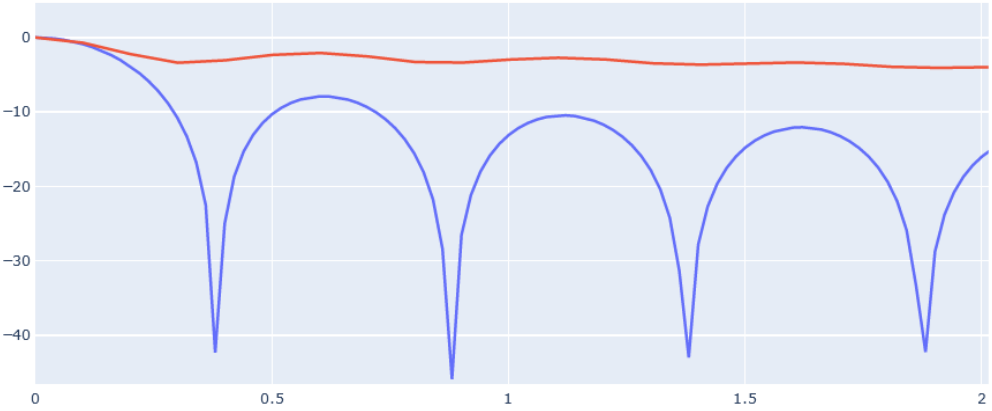

Figure 11: comparison of the average power in function of the distance between the UE and the default position of the UE (red) with the Bessel function of the first kind and zeroth order (blue).

3.3.2.2 Spacing of the base station antennas

Next, the spacing of the BS antennas will differ within the following plots. With more spacing between the BS antennas, the radiating near-field will again start further and further away. For the default setup, the UE is at the edge between the radiating and the reactive near-field if the spacing is approximately 0.5λ. Again, the radiation patterns shown in Figure 12 show a less directive pattern as the UE comes into the reactive near-field.

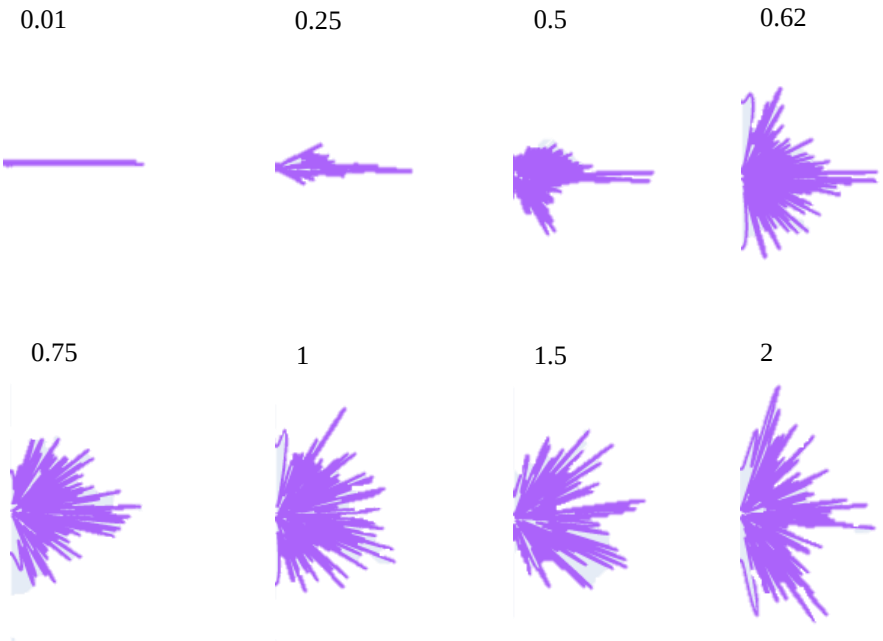

Figure 12: antenna patterns for different BS antenna spacings [λ]

If then the corresponding power patterns from Figure 14[5] are examined, it can be noted that the bubble first grows a bit and then gets smaller again. The more dM grows, the faster the plot seems to decorrelate. However, one needs to keep in mind that the BS antennas at the outside of the BS are much further away from the UE. Therefore, the path loss will be larger at some points. This can explain why the plots for a higher dM seem to go more often lower in power.

3.3.2.3 Placing of the scatterers

Some different placings of scatterers are then examined. To start, the scatterers are placed behind the UE, which means that there are no scatterers between the BS and the UE. As can be expected, Figure 13 shows that places that are closer to the scatterers get more power than the ones closer to the BS as there is (in this case erroneously) no LOS included. The shape of the bubble is also very non-circular as it is hard to form a circle with only beams coming from one side.

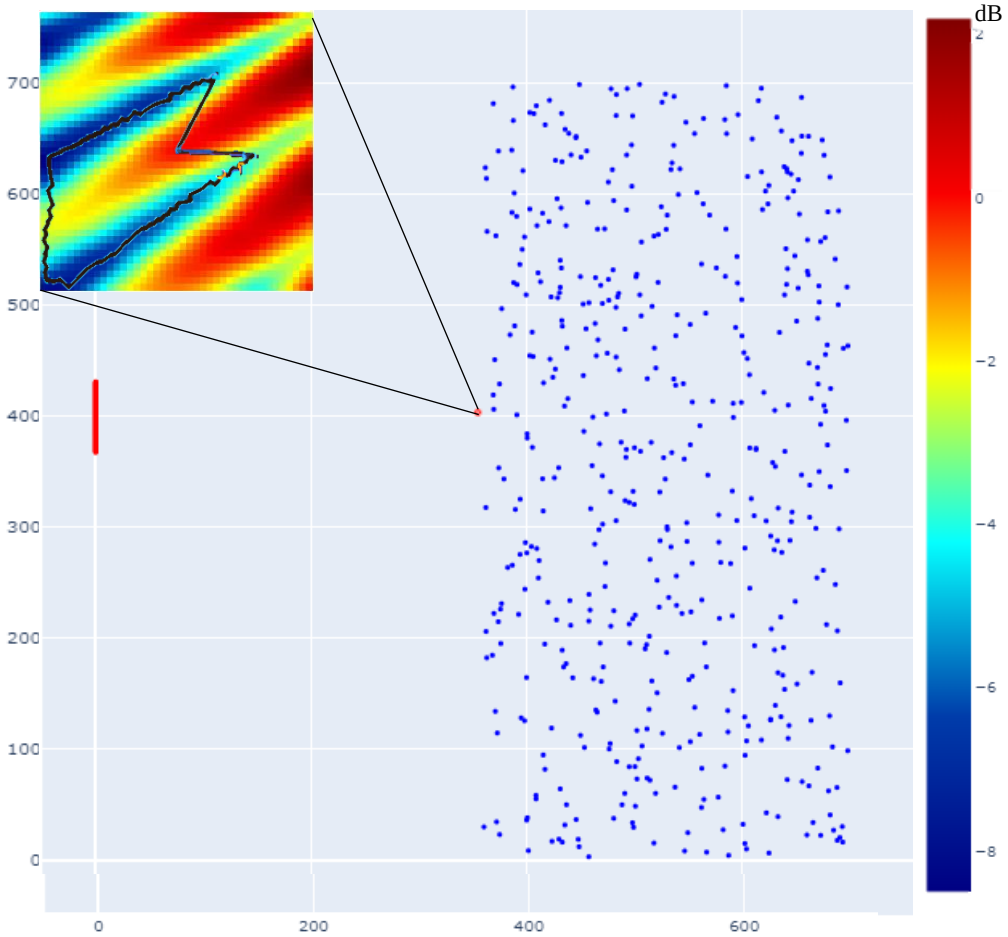

Figure 13: result for a setup with scatterers behind the UE

[5] All plots in Figure 14 are plotted 5λ around the default UE-position (354.62, 403.956). They also share the same colour scaling at the right of the figure.

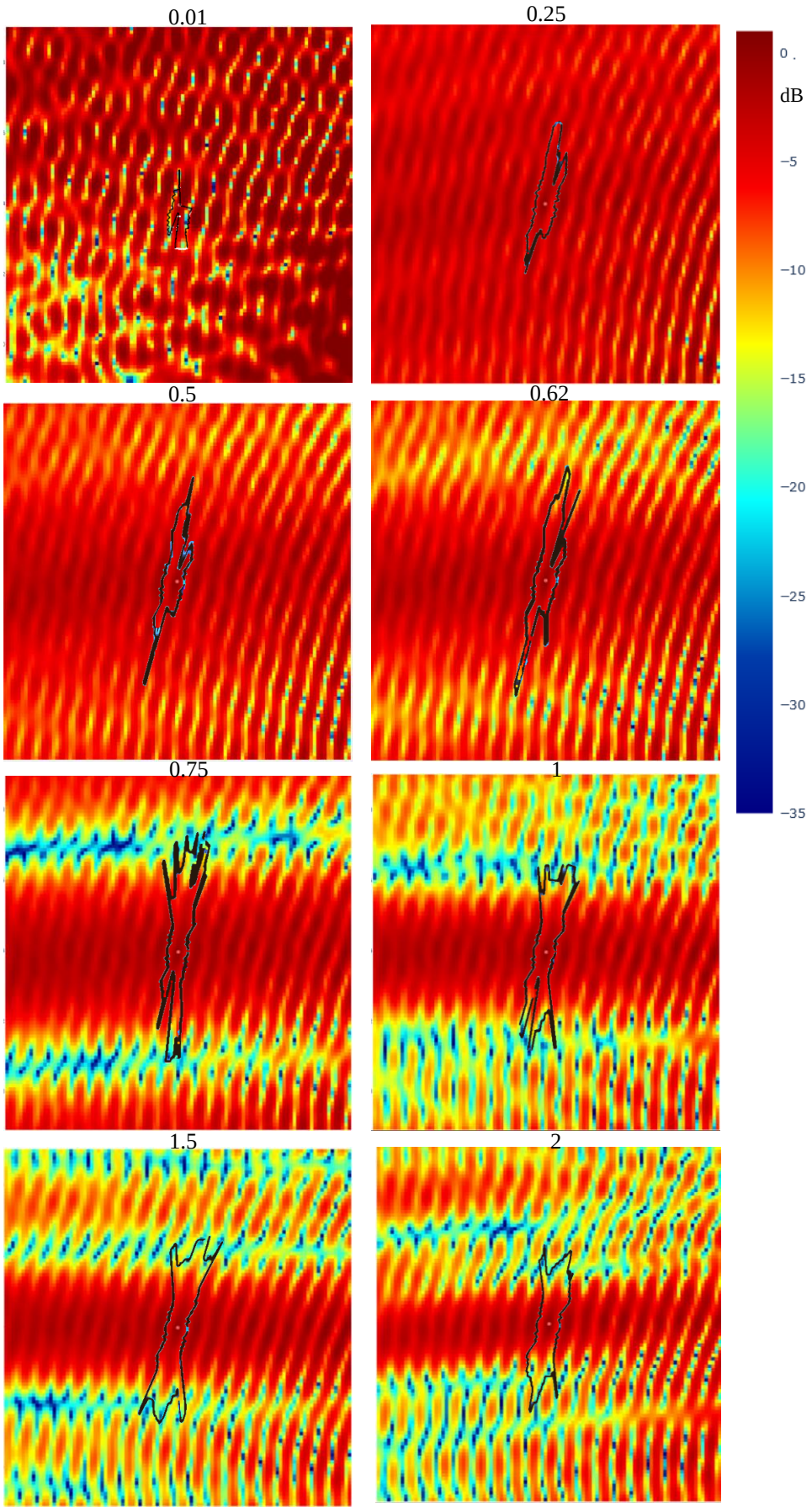

Figure 14: power pattern for different spacings of the BS antennas

The same can then be done with all scatterers at one side of the UE. More or less the same outcome would be expected, but this time bubbles can more or less be distinguished. This probably occurs because the shortest path between UE and BS is not via the scatterer that stands closest to the UE. Therefore two beams that are under a sufficiently different angle contribute almost the same to the formation of the bubble and the result comes closer to the default pattern found in Figure 6.

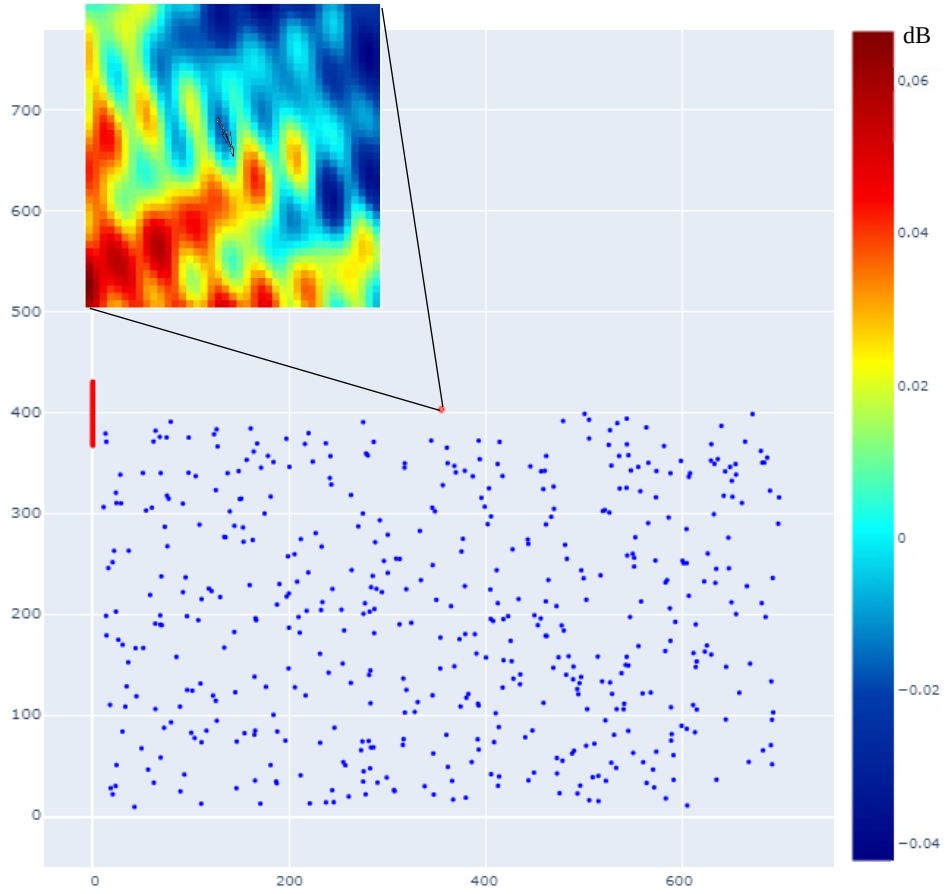

Figure 15: result for scatterers at one side of the UE

What would happen if all scatterers are placed very close to the UE? This setup should have more or less the same behaviour as when the scattering environment would be denser. The result is displayed in Figure 17 and shows that a more circular bubble is formed around the UE. Also, the angular power spread from Figure 16 seams more uniform than the one for the default settings.

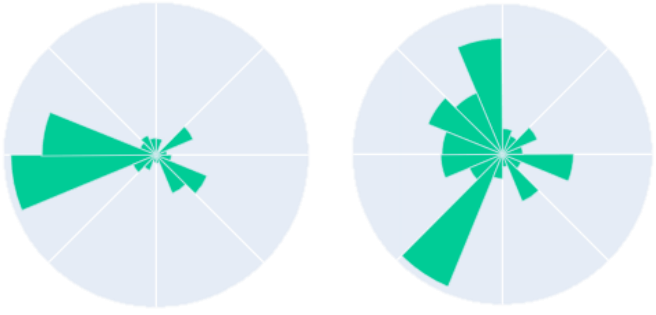

Figure 16: angular power spread for the default setup (left) and the dense setup (right)

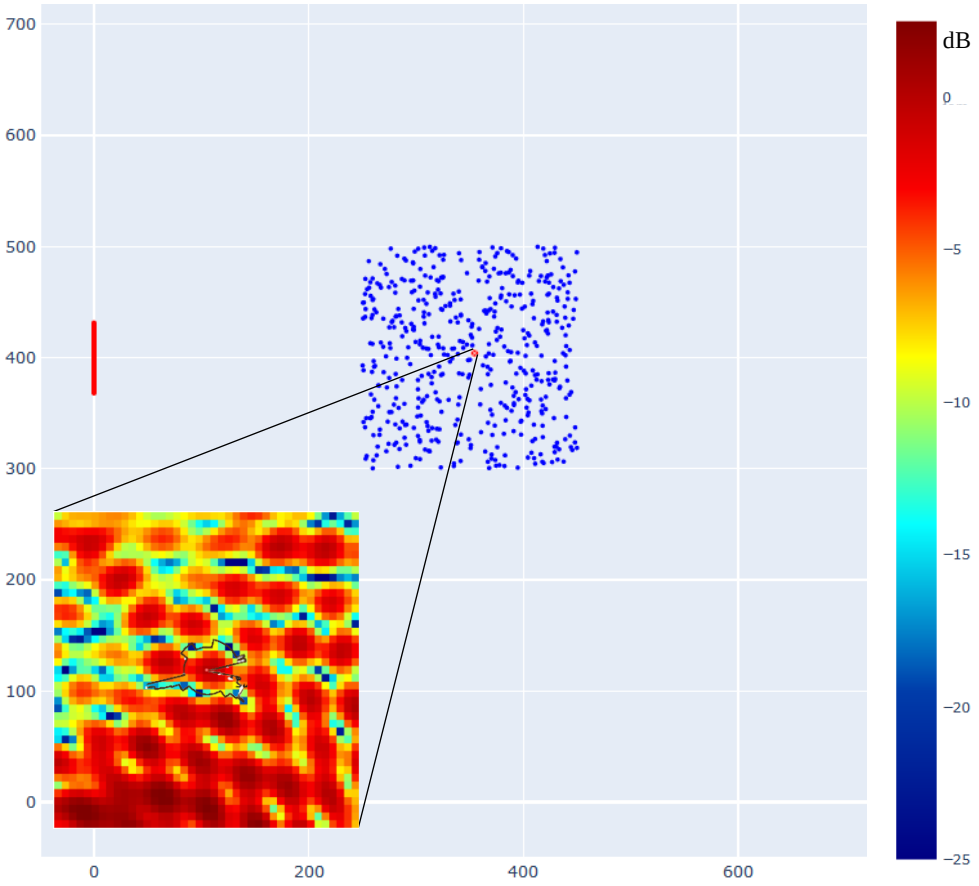

Figure 17: result for a denser scattering environment around the UE

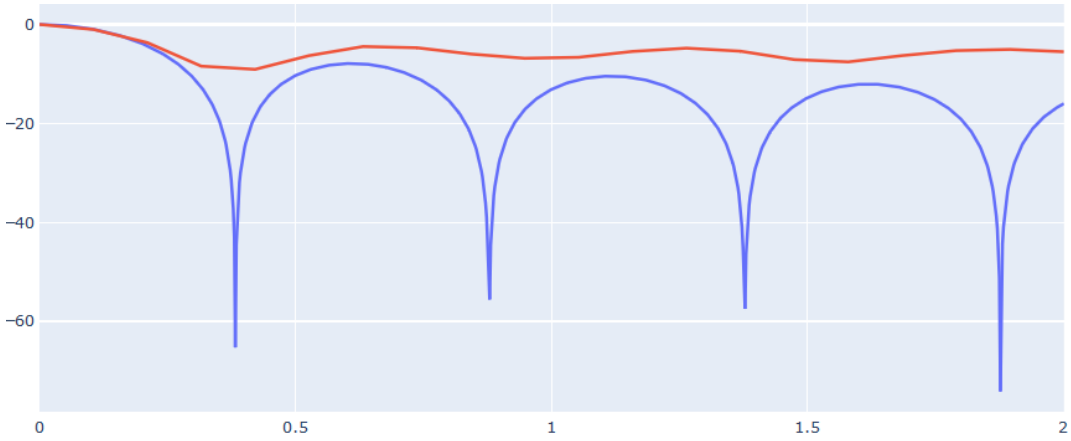

Figure 18: comparison of the average power [dB] in function of the distance between the UE and the default position of the UE (red) [λ] with the Bessel function of the first kind and zeroth-order (blue).

Further, a similar plot as Figure 11 can be made and compared with it. This is exhibited in Figure 18 and shows that the first hill falls off deeper, more like the Bessel function. Afterwards, on the other hand, the bumps don't follow the Bessel function as they did for the default setup. This last matter does however not affect the channel aging, so doesn't have to be taken into account in this thesis.

Some sidenotes have to be made for this setup. Imprimis, the area consisting of the UE and the scatterers stands far away from the BS. This is done so that it would be located outside of the reactive near-field. Furthermore, this setup is made so that the scattering becomes denser without increasing the calculation time by keeping S=500. This, however, might be seen as an unrealistic composition as, in reality, there will probably also be scatterers closer to the BS that have a meaningful addition to the result. Figure 19 is therefore created which shows that, considering that the scatterers are also placed differently, the result doesn't seem to differ as much. This shows that only scatterers that are close to the UE have a big impact on the received power.

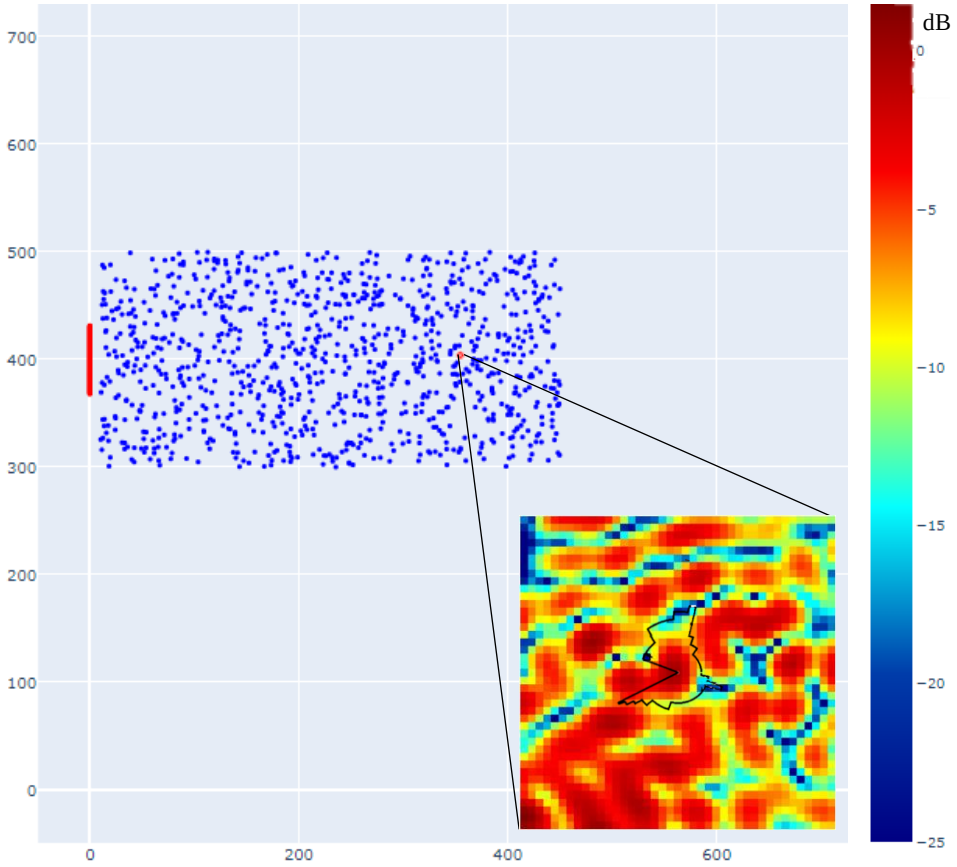

Figure 19: result for a denser scattering environment around the UE leaning closer to reality with S=1000

3.3.2.4 Placing of the user equipment

Finally, some different locations for the UE are tested. The first position is one that is not in front of the BS. As the result shows in Figure 20, there are no new elements that come up in comparison to the default setup. There is still a beam-like pattern in the direction of the BS and the power still rises closer to a scatterer.
Speaking of which, the next setup will be containing a UE that is positioned close to a scatterer from the beginning. A close-up for this result is shown in Figure 21. In this figure, it is clear that there is no question of a bubble around the UE as the bubble is more situated around the scatterer. The scatterer is in this plot not displayed but is located in the darkest red pixel of the plot.

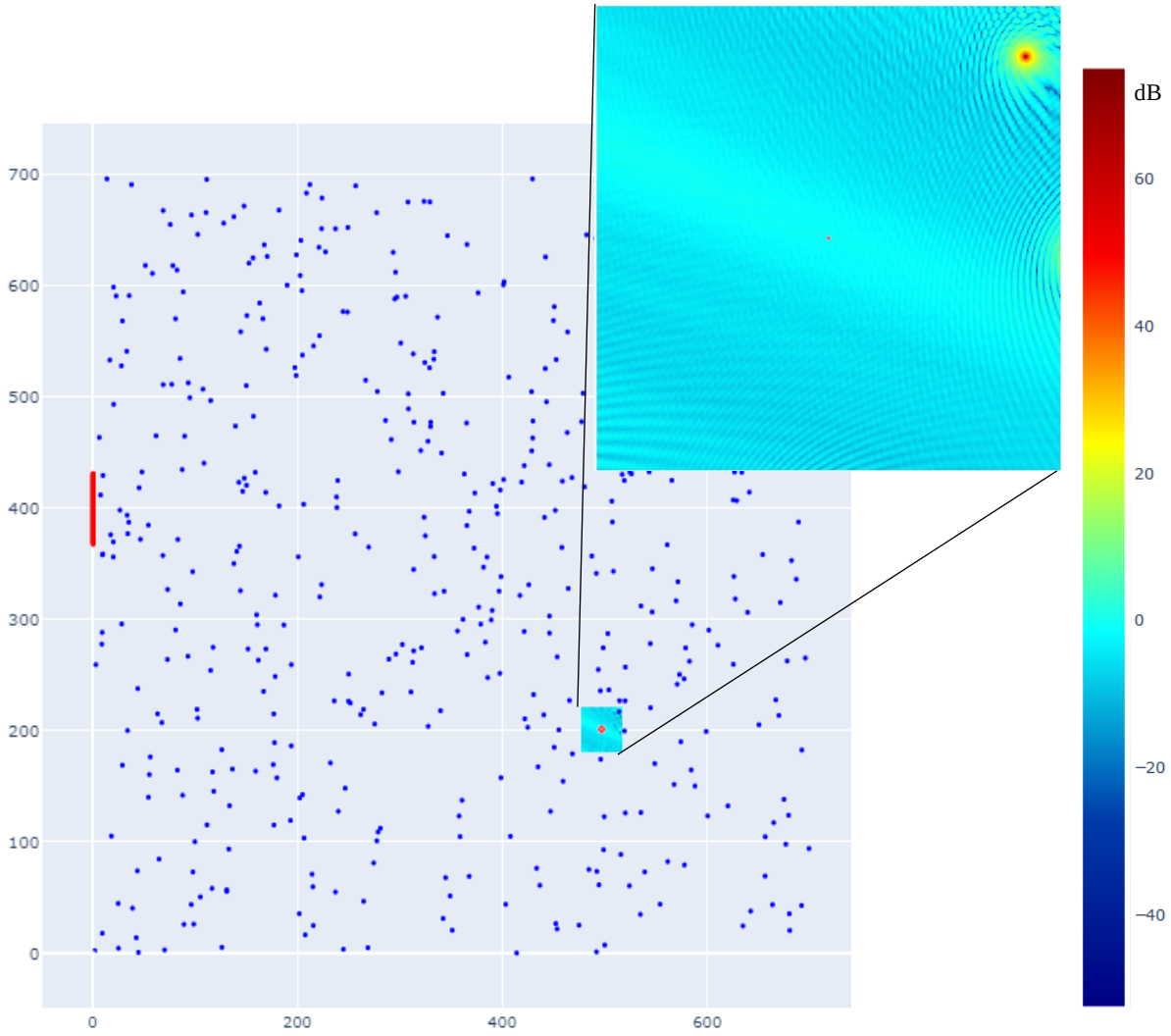

Figure 20: result for an UE not in front of the BS

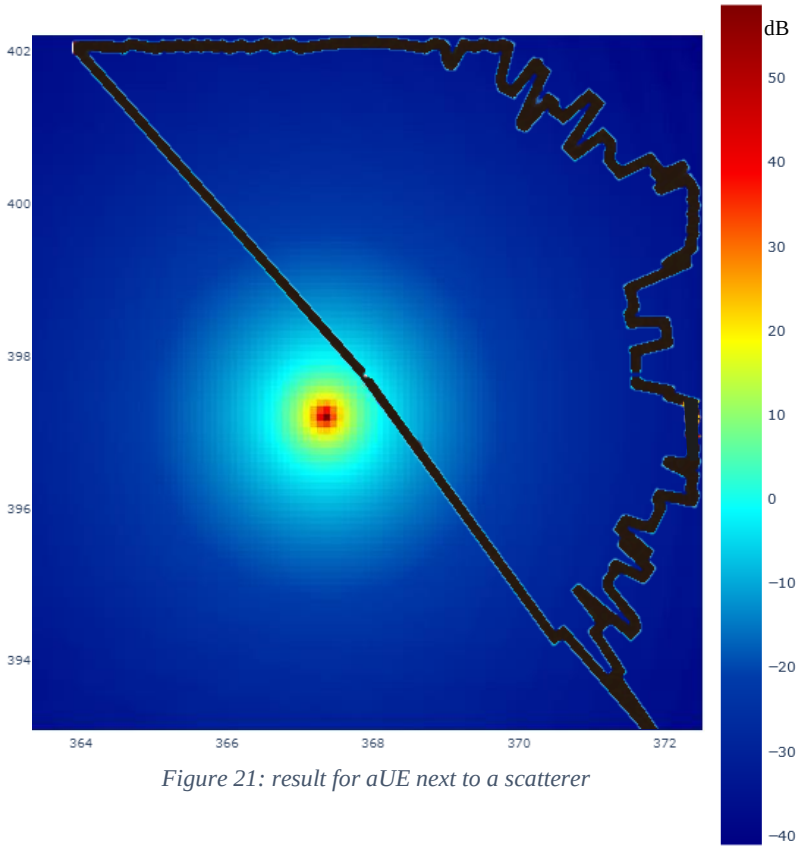

Figure 21: result for aUE next to a scatterer

4 Conclusion and future work

In this section, a conclusion is formed and some ideas for future work are explained. Some more simulation can be done but, evidently, also measurements should take place in the future. Some thoughts on that are also elaborated.

4.1 Conclusion

With this thesis was tried to form an image of what channel aging looks like in Massive MIMO for IIoT environments. A simulation model was created that stands as close to a realistic situation as possible, without getting too complex computationally.

For a linear antenna array in the BS, M=126 is a good choice although for the considered situations M=64 would not be much worse while the complexity of the BS would be smaller. With M=64, the reactive near-field also ends closer to the BS so fewer UEs would suffer from different behaviour. Also, the spacing of 0.62λ instead of 0.5 λ seems a strange choice as grating lobes start to appear and the near-field grows bigger again.
A denser and more uniformly spread scattering environment contributes to a pattern that stands closer to the theoretic model where the pattern more or less follows a Bessel function of the first kind and the zeroth-order.

4.2 Future work in the simulations

MRC might not be the best precoding technology after all. Therefore other precoding techniques should be worked out in the future. Also, some extra executions of the simulations done in this thesis might come in handy as the simulations in 3.3.2.1 don't cover all possible scenarios. Those in the rest of 3.3.2 are also just snapshots of a particular situation. Extra implementations would result in more measurable results that for example can give an answer to how far away a UE has to stay away from a scatterer in order to get its own bubble.

The simulations can, in addition, be more elaborated so that the area would be walled in, paths can consist of more scatterers, a LOS path can be included and maybe even some machinery or the like can be added to the model. Also, the behaviour of the scene with clustered scatterers or with more UEs in the field might be interesting to investigate.

Also, another array layout at the BS can be chosen in the simulations. As an IIoT environment is mostly one indoors, a planar BS might be a good choice. This not only makes the aperture of the array smaller, but also entails the possibility to work in both the elevation and the azimuth plane. As the calculations then become three dimensional, however, the computational complexity also grows and a different way of showing the results might have to be reconsidered.

4.3 Measurements

As the ultimate goal is to see what channel aging does in practice, a measurement campaign is inevitable. Following the perspective of this thesis and the previously planned measurements, the measurements preferably take place in a big (fabrics) hall. The BS is then mounted on a wall or in a corner. The higher the BS is mounted, the higher the chance that a LOS exists, although it's still quite unsure whether this is valued. The measurements can then start with a UE in an empty space after which more and more objects can be added.
It may be appropriate to let the UE move in a spiral path, starting from it’s starting position going outward as theoretically the bubble should be close to circular. Such a movement is for example possible by mounting the antenna on a 3D-printer or a similar robot so that the movement can be determined precisely.

List of abbreviations

(N)LOS	*(Non)-line-of-sight*
BS	*Base station*
CSI	*Channel State Information*
DoF	*Degrees of freedom*
FDD	*Frequency division duplexing*
IIoT	*Industrial Internet of Things*
IUI	*Inter-user interferences*
MF	*Matched Filtering*
MIMO	*Multiple input multiple output*
MMSE	*Minimum-Mean-Squared-Error*
MRC	*Maximum ratio combining*
MRT	*Maximum Ratio Transmission*
MU-MIMO	*Multi-user MIMO*
SDMA	*space-division multiple access*
TDD	*Time division duplexing*
UE	*User equipment*
ZF	*Zero-Forcing*

List of used symbols and notations

$\mathcal{N}_{\mathbb{C}}(\mu, \sigma^2)$	*Complex normal random variable with average μ and variation σ²*
dM	*Distance between BS antennas*
h	*Channel response*
K	*Number of UEs per cell*
M	*Number of antennas at the base station*
S	*Number of scatterers*
w	*Weight vector associated with a certain channel response*
ρ	*Correlation function in case of Rayleigh fading; associated with the zeroth-order Bessel function of the first kind.*

References

[1] "Reconfigurable Radio Network Platform (ReRaNP) - WISENET." https://wisenet.uia.no/projects/reconfigurable-radio-network-platform-reranp/ (accessed Aug. 01, 2020).

[2] E. Björnson, J. Hoydis, and L. Sanguinetti, "Massive MIMO Networks: Spectral, Energy, and Hardware Efficiency," *Foundations and Trends® in Signal Processing*, vol. 11, no. 3–4, pp. 154–655, 2017, DOI: 10.1561/2000000093.

[3] T. L. Marzetta, "Massive MIMO: An Introduction," *Bell Labs Technical Journal*, vol. 20, pp. 11–22, 2015, DOI: 10.15325/BLTJ.2015.2407793.

[4] B. M. Lee and H. Yang, "Massive MIMO With Massive Connectivity for Industrial Internet of Things," *IEEE Transactions on Industrial Electronics*, vol. 67, no. 6, pp. 5187–5196, Jun. 2020, DOI: 10.1109/TIE.2019.2924855.

[5] E. G. Larsson, "How Many Antennas are Useful?," 2016. http://ma-mimo.ellintech.se/2016/10/27/how-many-antennas-are-useful/ (accessed Jul. 18, 2020).

[6] D. Tse, *Fundamentals of Wireless Communication 1*. Cambridge University Press, 2004.

[7] S. ; Saunders and A. Zavala, *Antenna and Propagation for Wireless Communication Systems*, 2nd ed. Chichester: John Wiley & Sons Ltd, 2007.

[8] ITU-R, "Calculation of free-space attenuation," 2019. [Online]. Available: https://extranet.itu.int/brdocsearch/_layouts/15/WopiFrame.aspx?sourcedoc=%7B58b78669-0f51-41d6-99e9-b2063f3680d9%7D&action=view&wdAccPdf=0.

[9] C. A. Balanis, *ANTENNA THEORY | ANALYSIS AND DESIGN*, 4th ed. Hoboken: John Wiley & Sons, Inc, 2016.

[10] E. Björnson, E. G. Larsson, and T. L. Marzetta, "Massive MIMO: ten myths and one critical question," *IEEE Communications Magazine*, vol. 54, no. 2, pp. 114–123, Feb. 2016, DOI: 10.1109/MCOM.2016.7402270.

[11] E. Björnson, "Disadvantages with TDD," 2018. https://ma-mimo.ellintech.se/2018/06/22/disadvantages-with-tdd/ (accessed Jul. 18, 2020).

[12] X. Gao, "Massive MIMO in real propagation environments," 2016.

[13] J. Bai, "Synchronization and Channel Estimation in Massive MIMO Systems," 2016.

[14] K. T. Truong and R. W. Heath, "Effects of channel aging in massive MIMO systems," *Journal of Communications and Networks*, vol. 15, no. 4, pp. 338–351, 2013, DOI: 10.1109/JCN.2013.000065.

[15] M. M. Taygur and T. F. Eibert, “Analyzing the Channel Aging Effects on Massive MIMO Downlink by Ray-Tracing,” *IEEE International Symposium on Personal, Indoor and Mobile Radio Communications, PIMRC*, vol. 1, 2018, DOI: 10.1109/PIMRC.2018.8580703.

[16] “Introducing Massive MIMO Technology,” Jan. 12, 2018. https://www.4g-lte.net/technology/massive-mimo-technology/ (accessed Jul. 19, 2020).

[17] E. Björnson, “Massive MIMO for 5G below 6 GHz Achieving Spectral Efficiency, Link Reliability, and Low-Power Operation.” 2018, [Online]. Available: http://massive-mimo.net.

[18] F. Rusek *et al.*, “Scaling up MIMO : Opportunities and challenges with very large arrays,” *IEEE Signal Processing Magazine*, vol. 30, no. 1, pp. 40–60, 2013, DOI: 10.1109/MSP.2011.2178495.

[19] N. H. M. Adnan, I. M. Rafiqul, and A. H. M. Zahirul Alam, “Effects of inter element spacing on large antenna array characteristics,” *2017 IEEE International Conference on Smart Instrumentation, Measurement and Applications, ICSIMA 2017*, vol. 2017-Novem, no. November, pp. 1–5, 2018, DOI: 10.1109/ICSIMA.2017.8311993.

[20] J. Abraham and T. Ekman, “Power Inversion of the Massive MIMO Channel,” May 2019, [Online]. Available: http://arxiv.org/abs/1905.07555.

[21] “Carrier wave.” https://www.dictionary.com/ (accessed Jul. 19, 2020).